Biomaterials 165 (2018) 14–24

Contents lists available at ScienceDirect

Biomaterials

journal homepage: www.elsevier.com/locate/biomaterials

Hydrotalcite monolayer toward high performance synergistic dual-modal imaging and cancer therapy

Xuan Mei [a], Wei Wang [a], Liang Yan [a], Tingting Hu [a], Ruizheng Liang [a, *], Dan Yan [b, **], Min Wei [a, ***], David G. Evans [a], Xue Duan [a]

[a] State Key Laboratory of Chemical Resource Engineering, Beijing Advanced Innovation Center for Soft Matter Science and Engineering, Beijing University of Chemical Technology, Beijing 100029, PR China
[b] Beijing Shijitan Hospital, Capital Medical University, Beijing 100038, PR China

ARTICLE INFO

Article history:
Received 13 December 2017
Received in revised form
6 February 2018
Accepted 16 February 2018
Available online 19 February 2018

Keywords:
Layered double hydroxide
Gold nanoclusters
Theranostic
Magnetic resonance imaging
Fluorescence imaging
Photodynamic therapy

ABSTRACT

Recently, theranostic has drawn tremendous attention by virtue of the nanotechnology development and new material exploration. Herein, we reported a novel theranostic system by loading Au nanoclusters (AuNCs) and Chlorin e6 (photosensitizer, Ce6) onto the monolayer nanosheet surface of Gd-doped layered double hydroxide (Gd-LDH). The as-prepared Ce6&AuNCs/Gd-LDH exhibits a largely enhanced fluorescence quantum yield (QY) of 18.5% relative to pristine AuNCs (QY = 3.1%) as well as superior T_1 magnetic resonance imaging (MRI) performance ($r_1 = 17.57\ mM^{-1}s^{-1}$) compared with commercial MRI contrast agent (Gd(III)-1,4,7,10-tetraazacyclododecane-1,4,7,10-tetraacetic acid (Gd-DOTA): $r_1 \approx 3.4\ mM^{-1}s^{-1}$), resulting from a synergistic effect between AuNCs and Gd-LDH. In addition, both *in vitro* and *in vivo* therapeutic evaluations demonstrate an efficient dual-modality imaging guided anticancer performance, especially the synergetic enhanced magnetic resonance/fluorescence (MR/FL) visualization of tumor site. Therefore, this work demonstrates a successful paradigm for the design and preparation of LDHs monolayer-based theranostic material, which holds great promises in practical applications.

1. Introduction

Theranostics, which combines diagnostic and therapeutic moieties into a single platform, can realize simultaneous diagnosis and therapy, real-time monitoring of drug distribution/delivery, and assessment of the treatment efficacy [1–6]. With the development of nanotechnology, a variety of inorganic and organic nanomaterials have been explored as theranostic agents with great potential applications in biomedicine [7–12]. Although much progress has been made [13–17], how to integrate diagnostic and therapeutic agent into one formulation, even with a largely enhanced synergistic effect between each component, is vitally important for theranostics effectiveness but remains a challenge. Recently, ultrathin two-dimensional (2D) nanomaterials (*e.g.*, graphene, transition-metal dichalcogenides, hexagonal boron nitride, black phosphorus, etc.), have attracted considerable interest in theranostics, owing to their intriguing quantum size and surface property [18–21]. However, previous ultrathin nanomaterials synthesized *via* "top-down" mechanical-exfoliation strategy, show difficulties in a fine control over composition, size, thickness, and uniformity [22–24]. Therefore, developing a new drug formulation which affords imaging and therapeutic modality on the basis of 2D material design and synthesis exploration, a tunable composition and structure as well as excellent synergistic diagnosis and treatment can be achieved.

Layered double hydroxides (LDHs), whose structure is described by the general formula $[M^{2+}_{1-x}M^{3+}_{x}(OH)_2](A^{n-})_{x/n}\cdot mH_2O$ (M^{2+} and M^{3+} are divalent and trivalent cations, and A^{n-} is the charge-balancing interlayer anion), have attracted extensive attention as a 2D drug carrier [25–28]. A unique property of LDHs materials is that bulk LDHs microcrystals can be delaminated into monolayer nanosheets *via* top-down method [29–31], which have shown excellent performance in catalysis [32], electrochemistry [33] and energy storage [34], owing to the extremely high specific surface

* Corresponding author.
** Corresponding author.
*** Corresponding author.
E-mail addresses: liangrz@mail.buct.edu.cn (R. Liang), yand@bjsjth.cn (D. Yan), weimin@mail.buct.edu.cn (M. Wei).

https://doi.org/10.1016/j.biomaterials.2018.02.032
0142-9612/

area and quantum effect. However, LDHs monolayer serving as theranostic material is rarely studied due to the low efficiency "top-down" mechanical-exfoliation method. Exploration on a "bottom-up" strategy for the synthesis of LDHs monolayer and taking advantage of the versatility in both host layer and charge-balancing anion, which could be used as a nanocarrier to integrate diagnostic and therapeutic moieties. For instance, if a high magnetic moment metal ion (*e.g.*, Gd^{3+}) is doped into LDH monolayer and a fluorescence imaging agent (*e.g.*, Au nanoclusters (AuNCs)) is anchored onto the monolayer surface, a magnetic resonance/fluorescence (MR/FL) dual-modality imaging material can be obtained, which would take the following advantages: (i) the fully exposured Gd^{3+} in LDH monolayer will strongly promote the MR imaging performance; (ii) due to the electron-withdrawing effect of LDH monolayer [35], the fluorescence emission and stability of AuNCs would be greatly enhanced. In addition, anticancer drugs can be further introduced into AuNCs/Gd-LDH system based on a supermolecular interaction, so as to achieve a synergistic dual-modality imaging guided cancer treatment.

In this work, we report a novel theranostic system by immobilizing AuNCs and Chlorin e6 (photosensitizer, Ce6) on the surface of Gd-doped LDH monolayer nanosheets (Gd-LDH) (Scheme 1), and the resulting Ce6&AuNCs/Gd-LDH monolayer material exhibits excellent MR/FL dual-modal imaging and photodynamic therapy (PDT) performance toward cancer. Monolayer Gd-LDH nanosheets were fabricated by a new bottom-up synthetic method, with a fine control over metal composition and thickness. Such a theranostic system shows superior MRI property with a large longitudinal MR relaxivity value (r_1) of 17.57 $mM^{-1}s^{-1}$, which is much superior to commercially used MRI contrast agent Gd(III)-1,4,7,10-tetraazacyclododecane-1,4,7,10-tetraacetic acid (Gd-DOTA) ($r_1 \approx 3.4\ mM^{-1}s^{-1}$) [36]. Moreover, due to the electron-withdrawing effect of LDH matrix, the fluorescence quantum yield (QY) of AuNCs enhances significantly from 3.1% (pristine AuNCs in aqueous solution) to 18.5% (localized onto Gd-LDH). Structure-property studies reveal an electron transfer from AuNCs to LDHs monolayer, accounting for this synergistically enhanced MRI and fluorescence imaging behavior. In addition, *in vitro* studies show a largely boosted PDT performance of Ce6&AuNCs/Gd-LDH, with a 11.7-fold ROS enhancement relative to pristine Ce6. *In vivo* investigations exhibit both an excellent MR/FL dual-modality imaging and superior PDT toward tumor treatment.

2. Experimental section

2.1. Materials

$Mg(NO_3)_2 \cdot 6H_2O$, $Al(NO_3)_3 \cdot 9H_2O$, $Gd(NO_3)_3 \cdot 6H_2O$, $Eu(NO_3)_3 \cdot 6H_2O$, NaOH, $NaNO_3$, formamide were purchased from Aladdin Chemical. Co. Ltd (Shanghai, China). Reduced glutathione (GSH), hydrogen tetrachloroaurate hydrate ($HAuCl_4 \cdot 3H_2O$), 2,7-fichlorodihydrofluorescein diacetate (DCFH-DA), calceinacetoxymethyl ester (Calcein-AM), propidium iodide (PI) and 4′,6-diamidino-2-phenylindole (DAPI) were obtained from Sigma-Aldrich Company (St. Louis, MO, USA). Chlorin e6 (Ce6) was obtained from J&K Scientific (China). High glucose Dulbecco's modified Eagles medium (DMEM), 0.25% trypsin-EDTA and penicillin/streptomycin were purchased from Gibco (Invitrogen, Carlsbad, CA). Fetal bovine serum (FBS) was purchased from Excell Bio. Co., Ltd. (Shanghai, China) Phosphate-buffered saline (PBS) was purchased from Solarbio Science &Technology Co, Ltd (Beijing, China). All of the above chemicals were of analytical-grade and used without any further purification. Ultrapure water from a Milli-Q Millipore system was used in all the processes.

2.2. Synthesis of Gd-LDH monolayer nanosheets

In a typical synthesis of Gd-LDH monolayer nanosheets, solution A: $Mg(NO_3)_2 \cdot 6H_2O$ (0.0008 mol), $Al(NO_3)_3 \cdot 9H_2O$ (a mol) and $Gd(NO_3)_3 \cdot 6H_2O$ (b mol) dissolved in 20 mL of deionized water ($a + b = 0.0004$). Solution B: NaOH (0.006 mol) dissolved in 20 mL of deionized water. Solution C: $NaNO_3$ (0.0002 mol) dissolved in a solvent composed of deionized water (15 mL) and formamide (5 mL). Solution A and B were added drop by drop into solution C at 85 °C with stirring for 20 min. The obtained precipitation was washed with deionized water and ethanol for four times by centrifugation. Subsequently, the residual formamide in the Gd-LDH monolayer sample can be removed by a dialysis (8 kDa) treatment.

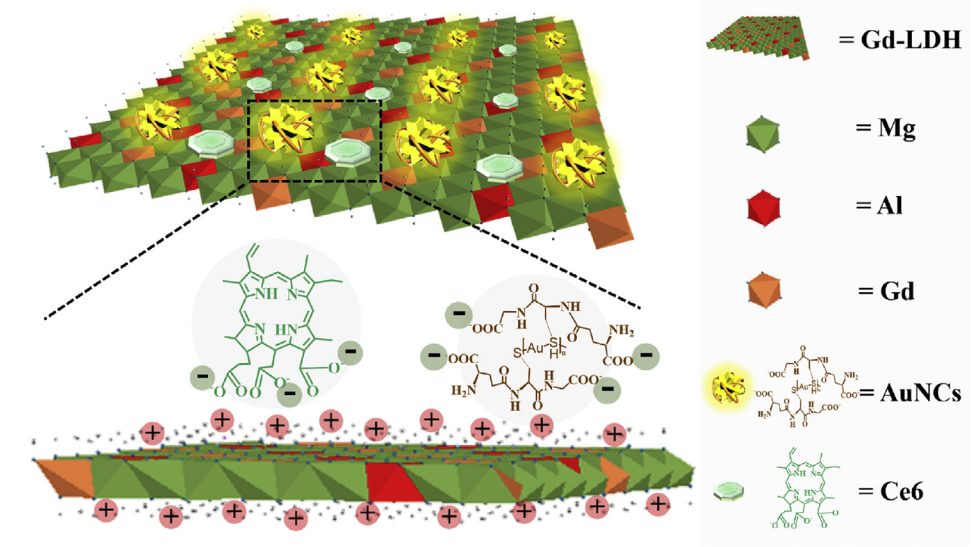

Scheme 1. Schematic illustration for the structure of Ce6&AuNCs/Gd-LDH.

2.3. Preparation of AuNCs and AuNCs/Gd-LDH

AuNCs was synthesized according to a reported method with some modifications [37]. Briefly, 1.80 mL of GSH (100 mM) was added into 58.2 mL of $HAuCl_4 \cdot 3H_2O$ (2.1 mM) and mixed thoroughly at room temperature. After further stirring for 20 min, the mixed solution was transferred to a stainless-steel Teflon-lined autoclave and reacted for 24 h (80 °C). After the autoclave was cooled down, extra reactants were removed by dialysis for 48 h and the obtained AuNCs was stored at 4 °C. To prepare $AuNCs_x$/Gd-LDH_y with different ratios, AuNCs sol (10 mM) was added dropwise into the Gd-LDH suspension (1 mM) with various molar ratios, and the resulting suspension was shaken continuously for another 20 min. The sample of AuNCs/Gd-LDH was obtained after centrifugation at 10000 r/min for 10 min.

2.4. Drug loading

0.1 mmol of Chlorin e6 (Ce6) was firstly dissolved in 10 mL of dimethyl sulfoxide (DMSO), and then 0.1 mL of Ce6 DMSO solution was added into 10 mL of AuNCs/Gd-LDH (concentration of Gd-LDH: 1 mM) suspension with stirring for 12 h. The excess Ce6 and DMSO were removed by centrifugation at 10000 r/min for 3 times, and then the Ce6&AuNCs/Gd-LDH was re-dispersed in water.

2.5. Detection of singlet oxygen production

The production efficiency of singlet oxygen was measured by using 1,3-diphenylisobenzofuran (DPBF) as a probe. A DPBF acetonitrile solution (20 μL, 70 μM) was added into 2 mL of Ce6, Ce6&AuNCs and Ce6&AuNCs/Gd-LDH solution, respectively, with equivalent Ce6 concentration (10 μg/ml). The mixed solution was irradiated by a simulated sunlight source (optical filter 650 ± 5 nm, 15 W/cm^2) for 8 min. UV−vis absorption spectra were recorded every minute and the decrease rate of absorption intensity at 410 nm is proportional to the singlet oxygen production efficiency.

2.6. T_1-weighted MRI study

MRI was performed on 7.0 T small animal MRI instrument. T_1-weighted MRI images of Gd-LDH and AuNCs/Gd-LDH were measured with different Gd concentrations of 0, 0.01, 0.02, 0.04, 0.06, 0.08 mM, respectively. MRI images were acquired using T_1 RARE sequence with parameters as follows: TR = 300 m s, TE = 6.06 ms, field of view = 45 mm × 45 mm, matrix size = 256 × 256, number of slices = 20, slice thickness = 1 mm, flip angle = 90° and NEX = 2.

2.7. Coordinated water molecules (q) measurement

The excited state lifetimes of Eu substituted complexes measured in H_2O and D_2O are associated with q by the equation: $q = A\ (t_{H2O}^{-1} - t_{D2O}^{-1})$ [38], in which A is a constant of 1.05 (water molecules) and t is the excited state lifetime. According to the reported method, Gd was substituted by Eu to determine the coordinated water molecules in Gd complexes due to the similar ionic radii [39]. To determine the number of coordinated water molecule in Gd-LDH and AuNCs/Gd-LDH, Eu-LDH monolayer was firstly synthesized with the same bottom-up method. Afterwards, the excited state lifetimes Eu-LDH and AuNCs/Eu-LDH were measured in H_2O and D_2O, respectively. Finally, the number of q for Gd-LDH and AuNCs/Gd-LDH was calculated by the above equation.

2.8. Cell line and culture

HepG2 cells were purchased from Institute of Basic Medical Sciences Chinese Academy of Medical Sciences (Beijing, China) and incubate in 25 cm^2 cell-culture flask at 37 °C with an atmosphere of 5% CO_2. 10% fetal bovine serum (FBS) and 1% penicillin-streptomycin were added into Dulbecco's modified Eagle's medium (DMEM) as culture medium. 1.0 mL of trypsin (0.25%) was used to detach cells when they cover 80%–90% of bottom area and the process was terminated in 2 min by adding 2 mL DMEM.

2.9. In vitro fluorescence image

To study the *in vitro* fluorescence imaging, HepG2 cells were grown and expanded on 35 mm confocal dishes for 24 h. After incubating with pristine AuNCs, AuNCs/Gd-LDH, Ce6&AuNCs/Gd-LDH (equivalent AuNCs: 10 μg/mL) for 6 h, the cells were washed with PBS for 3 times sufficiently. The nuclei of cells were stained with 4′,6-diamidino-2-phenylindole (DAPI) for 10 min and washed with PBS again for 3 times. The fluorescent images were obtained by a Leica confocal laser scanning microscopy (Leica, Germany).

2.10. In vitro photodynamic therapy

HepG2 cells were seeded in two 96-well plates at the density of 1×10^4 cells/well and cultured overnight. Cells were incubated with 100 μL medium containing serious of pristine Ce6 (0–10 μg/mL), Ce6&AuNCs and Ce6&AuNCs/Gd-LDH (equivalent Ce6 0–10 μg/mL) for 24 h. After washing with PBS for 3 times, one plate was kept in the dark for dark toxicity study, and the other plate was irradiated with a simulated sunlight source (optical filter 650 ± 5 nm) at a power of 15 mW/cm^2 for 20 min. Afterwards, cells were grown for another 6 h before the standard methyl thiazolyl tetrazolium (MTT) assay. Both the dark toxicity and phototoxicity were evaluated by a standard MTT assay. The cell viability was calculated by the equation: Cell viability= (OD 490 nm of the experimental group/OD 490 nm of the control group) × 100%, where the cell viability of control group was denoted as 100%. Additionally, Calcein-AM and propidium iodide (PI) were used to stain the population of viable and necrotic cells.

2.11. Cellular ROS detection

HepG2 cells were incubated with Ce6 (5 μg/mL), Ce6&AuNCs and Ce6&AuNCs/Gd-LDH (equivalent 5 μg/mL of Ce6) for 24 h in 6-well plates. After washing with PBS, DCFH-DA (2×10^{-5} M) was added and incubated for 20 min. After irradiating with a simulated sunlight source (optical filter 650 ± 5 nm) at a power of 15 mW/cm^2 for 20 min, the generated ROS inside the cells was measured by flow cytometer quantitatively and imaged by a Leica confocal laser scanning microscopy.

2.12. Animal experiments

Male Balb/c mice (Balb/c-nude, aging 4–6 weeks) were purchased from Beijing Vital River Laboratory Animal Technology Co., Ltd and used under protocols approved by Beijing Shijitan Hospital Animal Research Center. 1×10^7 HepG2 cells suspended in 100 μL of phosphate buffered saline (PBS) were subcutaneously injected into the back of each mouse. All the experiments began when the tumor volume reached 70 mm^3.

2.13. In vivo MRI study

For *in vivo* MRI, mice were injected intravenously with Gd-LDH and AuNCs/Gd-LDH (equivalent Gd at 0.88 mg/kg of mice body weight), respectively. MRI images were acquired using T_1 RARE sequence with parameters as follows: TR = 500 ms, TE = 9 ms, field of view = 3 cm × 3 cm, matrix size = 256 × 256, number of slices = 20, slice thickness = 1 mm, flip angle = 180° and NEX = 4.

2.14. In vivo fluorescence imaging

Free AuNCs, AuNCs/Gd-LDH, and Ce6&AuNCs/Gd-LDH in 1 × PBS solution (200 μL, with a dosage of 2.2 mg AuNCs/kg of mouse body weight) were intratumorally injected into the tumor-bearing mice. Time-course fluorescent images (excitation: 410 nm; emission: 525–600 nm) were acquired on a IVIS lumina fluorescence imaging system. All the post injection images were captured at the same parameter settings and scale.

2.15. In vivo photodynamic therapy

Mice were randomized into six groups as follows (6 animals per group): (Group i) 200 μL of PBS without irradiation; (Group ii) 200 μL of Ce6 (2 mg/kg) without irradiation; (Group iii) 200 μL of Ce6&AuNCs/Gd-LDH (equivalent Ce6 2 mg/kg) without irradiation; (Group iv) 200 μL of PBS with irradiation; (Group v) 200 μL of Ce6 (2 mg/kg) with irradiation; (Group vi) 200 μL of Ce6&AuNCs/Gd-LDH (equivalent Ce6 2 mg/kg) with irradiation. Mice were irradiated by a helium-neon (He-Ne) laser (optical filter 650 ± 5 nm) at the power of 15 mW/cm^2 for 20 min. The tumor size was measured by a caliper every two days and calculated in the formula: volume= (tumor length) × (tumor width)^2 × 0.5. Relative tumor volume was calculated as V/V_0 (V and V_0 are the tumor volume measured at time t and t_0, respectively).

2.16. Histology examination

For histological examination, tumors and main organs from the treated group and control groups were fixed in 4% formalin and conducted with paraffin embedded sections for H&E staining. The slices were examined by a digital microscope (Leica). For blood analysis, 200 μL of blood was collected from mice treated with PBS and Ce6&AuNCs/Gd-LDH after intravenously injection for 1 day and 7 days, respectively. The blood was separated and analyzed under standard biochemical examination.

2.17. Sample characterization

Powder X-ray diffraction patterns of the samples were collected on a Shimadzu XRD-6000 diffractometer using a Cu Kα source, with a scan step of 0.02° and a scan range between 3° and 70°. The morphology of the samples was investigated using a scanning electron microscope (SEM; Zeiss SUPRA 55) with an accelerating voltage of 20 kV. High resolution transmission electron microscope (HRTEM) images were recorded with JEOL, JEM-2100; the accelerating voltage was 200 kV. The chemical composition of LDH samples were determined by inductively coupled plasma (ICP) emission spectroscopy on a Shimadzu ICPS-7500 instrument. The particle size distribution was determined using a Malvern Mastersizer 2000 laser particle size analyzer. The Fourier transform infrared (FT-IR) spectra were recorded in the range 4000–400 cm^{-1} with 2 cm^{-1} resolution on a Vector 22 (Bruker) spectrophotometer. The UV–vis absorption spectra were collected in the range 250–700 nm on a Shimadzu U-3000 spectrophotometer, with a slit width of 1.0 nm. The fluorescence spectra were performed on a RF-5301PC fluorospectrophotometer with the excitation wavelength of 400 nm. The fluorescence emission spectra range in 470–700 nm, and the width of both the excitation and emission slit is 1.5 nm. Fluorescence images of these samples were obtained using a Leica confocal laser scanning microscopy. *In vivo* images were obtained using an IVIS Lumina fluorescence imaging system. The MRI experiments were conducted on a Bruker PharmaScan device. The blood cell counts and serum biochemistry analysis were measured on an automated hematology analyzer (Bayer Advia 2120) and automatic biochemical analyzer (Olympus AU400), respectively.

3. Results and discussion

3.1. Structural and morphological characterization of Gd-LDH nanosheets

To prepare the monolayer Gd-LDH nanosheets, a one-step bottom-up synthetic method was developed, in which Al^{3+} in MgAl-LDH was partially substituted by Gd^{3+} during the synthesis process. The doping content of Gd^{3+} was investigated from 10% to 60% (molar ratio of $Gd^{3+}/(Gd^{3+}+Al^{3+})$), and all these samples showed the (003), (006), (009) and (110) reflection of an LDH phase (Fig. S1). However, the diffraction intensity decreases along with the increase of Gd^{3+} content, and Gd-LDH nanosheets sample with 60% doping gives a rather poor crystal structure. Thus, the highest ratio of doped Gd^{3+} is determined to be 50%. These Gd-LDH nanosheets samples with 10%–50% Gd^{3+} doping display no obvious difference both in zeta potential (Fig. S2: ranging from 21 to 47 mV) and size distribution (Fig. S3: ranging from 60 to 110 nm). Moreover, the molar ratios of Mg/Al/Gd measured by inductively coupled plasma optical emission spectrometry (ICP) give rather close values to the nominal ones (Table S1). For a comparative study, the sample of bulk LDH was synthesized by co-precipitation method with the highest Gd-doping of 21.1% according to the ICP result (Table S2). A large doping up to 30% leads to deterioration in morphology, zeta potential and size distribution of bulk Gd-LDH (Fig. S4 and S5), in contrast to the monolayer sample with a Gd-doping as high as 50%.

HRTEM image of Gd-LDH monolayer shows a plate-like morphology with a lateral dimension of ~50 nm, and a lattice fringe of 0.178 nm corresponds to the [110] plane of an LDH phase (Fig. 1A and inset). The thickness of Gd-LDH monolayer, studied by atomic force microscope (AFM), is determined to be ~1.2 nm (Fig. 1B and C), close to the theoretical value of an LDH monolayer (~0.9 nm). In addition, the monolayer structure of Gd-LDH nanosheet was studied by XRD measurement. As shown in Fig. S6, the LDHs bulk sample (Fig. S6, blue line) shows a typical (003) reflection of an LDHs phase at 2θ 11.66°; while this is not observed for the Gd-LDH monolayer colloid sample (Fig. S6, green line), indicating the lack of long-range-ordered layered structure [40]. Moreover, the (003) reflection at 2θ 11.68° appears again after drying the Gd-LDH monolayer colloid sample, which is ascribed to the re-stacking of LDH monolayer to bulk state (Fig. S6, red line). Subsequently, AuNCs modified by glutathione ligand (average particle size: ~2 nm, Fig. S7), were immobilized onto the surface of Gd-LDH monolayer sample *via* a facile deposition method (see experimental section for details). A series of $AuNCs_x/Gd\text{-}LDH_y$ samples were prepared by changing the molar ratio of AuNCs to Gd-LDH, and HRTEM images showed an obviously enhanced density of AuNCs as x/y ratio increased from 0.1 to 3 (Fig. S8).

Representative HRTEM images of $AuNCs_2/Gd\text{-}LDH_1$ sample are shown in Fig. 1D, from which numerous AuNCs are located on the surface of lamellar Gd-LDH without altering the hexagonal plate-like morphology. A lattice fringe of 0.232 nm is determined (Fig. 1D, inset), which is attributed to the typical [111] phase of

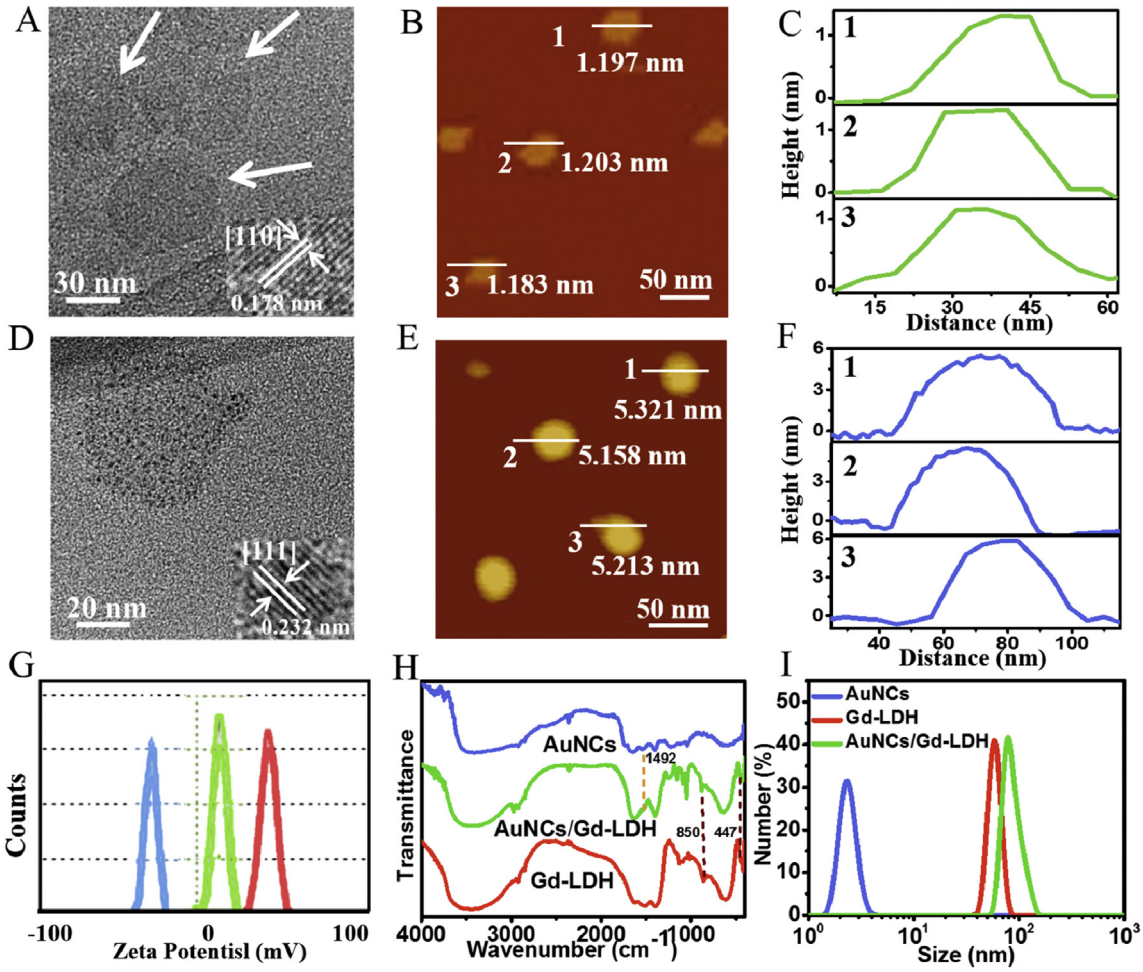

Fig. 1. (A) HRTEM image of monolayer Gd-LDH. The inset shows the [110] crystal lattice of an LDH phase, (B) AFM image and (C) thickness measurement for monolayer Gd-LDH (1, 2, 3 denotes three representative particles). (D) HRTEM image, (E) AFM image and (F) thickness measurement for AuNCs localized onto monolayer Gd-LDH (AuNCs/Gd-LDH; 1, 2, 3 denotes three representative particles). (G) Zeta potential, (H) FT-IR spectra and (I) particle size distribution of AuNCs, monolayer Gd-LDH and AuNCs/Gd-LDH.

AuNCs. The combination of AuNCs and Gd-LDH monolayer is clearly confirmed in Fig. S9, where the lattice fringes of both AuNCs [111] and LDH [110] are detected within the same visual field. AFM images (Fig. 1E and F) show a thickness of ~5.2 nm for AuNCs/Gd-LDH, which can be attributed to the immobilization of AuNCs on both sides of Gd-LDH monolayer. The change in zeta potential also demonstrates the localization of AuNCs onto Gd-LDH: with the increase of x/y ratio from 0.1 to 3, the zeta potential of $AuNCs_x$/Gd-LDH_y samples decreases from 34.2 mV to 16.3 mV (Fig. S10 and Fig. 1G, green line), which is ascribed to the immobilization of negatively-charged AuNCs (Fig. 1G, blue line, −23.5 mV) onto positively-charged Gd-LDH (Fig. 1G, red line, 35.7 mV). Therefore, electrostatic interaction (as shown in the change of zeta potential) as well as hydrogen bonding (between carboxyl group of AuNCs and hydroxyl group of Gd-LDH nanosheets) result in the efficient anchoring of AuNCs onto Gd-LDH nanosheets. In addition, FT-IR spectra further proves the combination of AuNCs and Gd-LDH (Fig. 1H), in which AuNCs/Gd-LDH sample exhibits both the characteristic band of AuNCs at 1492 cm^{-1} (the vibration of C−S) as well as Gd-LDH at 447 cm^{-1} (vibration of O−H) and 850 cm^{-1} (vibration of metal−O bond). As shown in Fig. 1I, the hydrodynamic diameter of AuNCs/Gd-LDH (blue line) is ~80 nm according to DLS measurements, in contrast to that of Gd-LDH monolayer (red line, ~60 nm).

3.2. Fluorescence and MRI properties of $AuNCs_x$/Gd-LDH_y samples

The photoluminescence properties of various $AuNCs_x$/Gd-LDH_y were investigated. Fig. 2A shows the UV−vis absorption spectra of these samples, in which the absorption at ~400 nm ascribed to AuNCs enhances gradually from $x/y = 0.1$: 1 to $x/y = 2$: 1, and no further increase is found for $x/y = 3$: 1, indicating the saturated loading capacity at $x/y = 2$: 1. Fig. 2B displays the fluorescence spectra of pristine AuNCs and $AuNCs_x$/Gd-LDH_y samples. Pristine AuNCs gives a rather weak fluorescence intensity; an increased intensity of $AuNCs_x$/Gd-LDH_y is observed from $x/y = 0.1$: 1 to $x/y = 2$: 1. However, the intensity decreases from $x/y = 2$: 1 to 3: 1, which is ascribed to the self-quenching resulting from enhanced gold−gold interactions between adjacent AuNCs [41,42]. Such a phenomenon was further quantified by quantum yield (QY) measurements. As illustrated in Fig. 2C, the highest QY value is obtained for the sample of $AuNCs_2$/Gd-LDH_1 (18.5%), which is ~6.6 folds larger than pristine AuNCs (3.1%). The photographs of all these samples under UV light irradiation were recorded (Fig. 2C, inset), which showed a similar variation tendency in fluorescence intensity. The excitation-state lifetime of $AuNCs_2$/Gd-LDH_1 reaches to ~15.1 μs, which is 7 times longer than that of pristine AuNCs (~1.99 μs) (Fig. S11). Moreover, the comparison of stability against photobleaching was performed between pristine AuNCs and

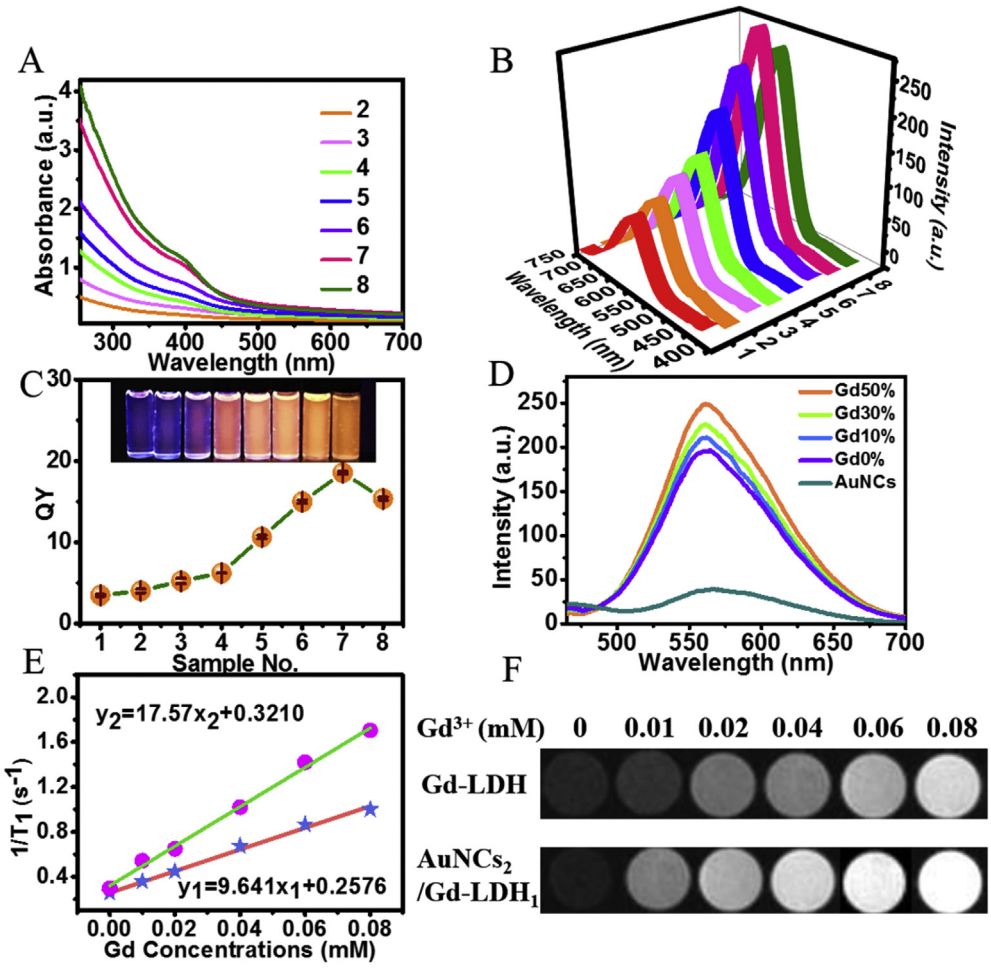

Fig. 2. (A) UV–vis absorption spectra, (B) fluorescence spectra and (C) absolute QY of $AuNCs_x$/Gd-LDH_y with equivalent Au (from Sample 1 to 8): $x/y = 1$: 0, 0.1: 1, 0.25: 1, 0.5: 1, 1: 1, 1.5: 1, 2: 1 and 3: 1, respectively. (D) Fluorescence spectra of $AuNCs_2$/Gd-LDH_1 with Gd-doping from 0 to 50%. (E) T_1-weighted relaxivity and (F) T_1-weighted MRI images of Gd-LDH and $AuNCs_2$/Gd-LDH_1 with various Gd concentrations, respectively.

AuNCs/Gd-LDH. The photographs in Fig. S12 show that the luminescence intensity of pristine AuNCs was bleached within 12 h under UV light irradiation while that of AuNCs/Gd-LDH maintained unchanged even after 24 h continuous irradiation. We further investigated the influence of Gd content on the fluorescence property of $AuNCs_2$/Gd-LDH_1. It's interesting that the fluorescence intensity increases gradually along with the increment of Gd content from 0% to 50% (Fig. 2D). This is probably ascribed to the electron interaction between of Gd^{3+} and AuNCs, which will be discussed in the next section.

In addition, the *in vitro* T_1-weighted relaxivity (r_1, the magnetic relaxation enhancement of the neighboring water protons, which determines MRI efficiency) of Gd-LDH and AuNCs/Gd-LDH was investigated. Notably, as shown in Fig. 2E, the T_1-weighted relaxivity increases significantly from 9.641 $mM^{-1}s^{-1}$ (Gd-LDH) to 17.57 $mM^{-1}s^{-1}$ (AuNCs/Gd-LDH), demonstrating that the loading of AuNCs remarkably improves the MRI sensitivity of Gd-LDH monolayer. This value is ~5.2 fold larger than that of commercial MRI contrast agent Gd-DOTA (~3.4 $mM^{-1}s^{-1}$). Moreover, the r_1 values of Gd-LDH and AuNCs/Gd-LDH are larger than that of bulk Gd-LDH (6.233 $mM^{-1}s^{-1}$, Fig. S13). The T_1-weighted MR images of Gd-LDH and AuNCs/Gd-LDH are presented in Fig. 2F, showing an enhanced brightness as the Gd concentration increases from 0 to 0.08 mM.

The results above demonstrate that a significant synergistic effect occurs between MRI performance of Gd-LDH monolayer and fluorescent characteristic of AuNCs, which is very rare in dual- or multi-mode imaging systems. Previous studies have shown that the luminescent property of AuNCs originates from Au(I)–thiol species and its concentration determines the fluorescent performance [43]. Herein, X-ray photoelectron spectroscopy (XPS) was employed to investigate the valence state of AuNCs in the AuNCs/Gd-LDH. As shown in Fig. 3A, both pristine AuNCs and AuNCs/Gd-LDH show two peaks at 85.2 eV and 84.1 eV, which are attributed to Au(I)–thiol portion (blue line) and Au(0) nanocrystals (green line), respectively. The content of Au(I)–thiol increases markedly from ~32.5% (pristine AuNCs) to 56.1% (AuNCs/Gd-LDH); moreover, this proportion further increases from 56.1% to 73.4% as the Gd-doping rises from 0% to 50% (Fig. 3B–E). Fig. 3F displays the Au(I)–thiol concentration in AuNCs as a function of Gd-doping in Gd-LDH monolayer, which gives a similar change tendency toward QY. In addition, XPS spectra of Gd 3*d* and O 1*s* were studied. The binding energies of O 1*s* in OH^- group of Gd-LDH decreases from 531.9 eV to 530.8 eV with the increment of Gd ratio from 0% to 50% (Fig. 3G and I, left column); while Gd $3d_{3/2}$ and $3d_{5/2}$ decrease from 1220 eV to 1219 eV and from 1188 eV to 1187 eV (Fig. 3H and I, right column), respectively. The results indicate that this system undergoes an electron transfer from AuNCs to Gd^{3+} through hydroxyl group,

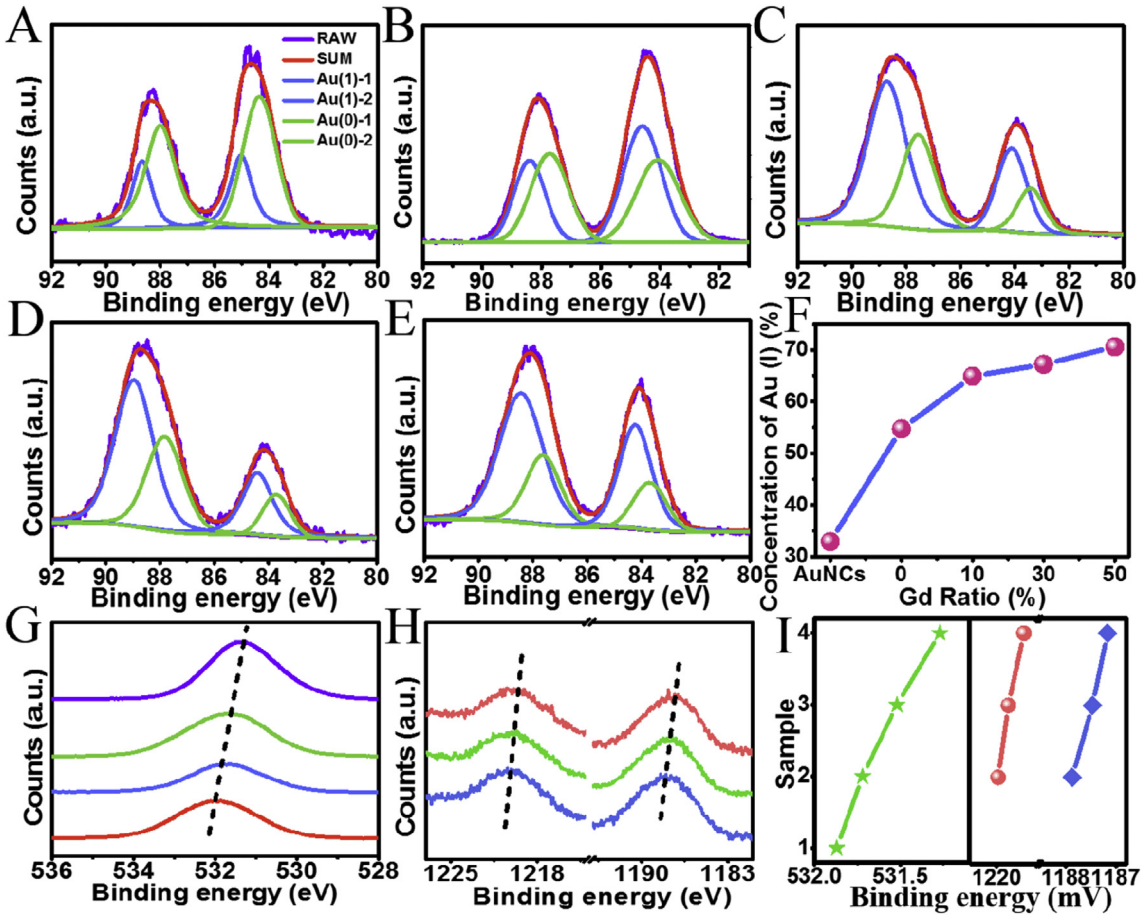

Fig. 3. XPS spectra of (A) pristine AuNCs; from (B) to (E): AuNCs/Gd-LDH with Gd ratio of 0, 10%, 30% and 50%, respectively. (F) Concentration of Au(I)—thiol in above samples as a function of Gd ratio in Gd-LDH. XPS spectra of (G) O 1*s*, (H) Gd 3*d*, and (I) binding energies of O 1*s* (left column) and Gd 3*d* (right column) for AuNCs/Gd-LDH (Sample 1 to 4: Gd ratio = 0%, 10%, 30% and 50%, respectively).

which leads to the increase of Au(I)—thiol portion and promotes the fluorescence quantum yield.

Subsequently, we further studied the reason for enhanced MRI of AuNCs/Gd-LDH. It has been reported that the performance of Gd(III)-based MRI contrast agents is highly dependent on the number of coordinated water molecules (q) in the first coordination sphere of Gd(III) ion, which can shorten the proton relaxation time of ambient water [44,45]. Herein, the value of q was determined according to a commonly used luminescence lifetime measurements (Fig. S14; see experimental section for details) [46,47]. The results show both q values of Gd-LDH (3.03) and AuNCs/Gd-LDH (3.23) are significantly larger than that of commercial MRI contrast agents ($q = 1.0$), which is responsible for the enhancement of longitudinal MR relaxivity (r_1). Moreover, AuNCs/Gd-LDH shows a 1.82-fold enhancement in T_1-weighted relaxivity compared with Gd-LDH. The magnetization curves at room temperature were measured to illustrate the magnetic behavior of LDH (without Gd-doping), AuNCs/LDH, Gd-LDH and AuNCs/Gd-LDH. As shown in Fig. 4A, LDH shows diamagnetic behavior, and AuNCs/LDH displays a weak ferromagnetic property. Interestingly, after the Gd(III) doping, Gd-LDH changes to paramagnetic with a magnetic susceptibility of 3.47 emu/(g·Oe) (Fig. 4B, blue line), due to the strong

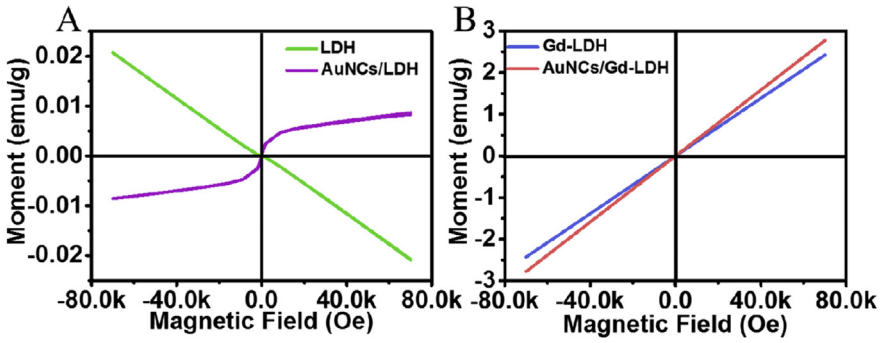

Fig. 4. Magnetization curves at 300 K for (A) LDH (without Gd-doping) and AuNCs/LDH, (B) Gd-LDH and AuNCs/Gd-LDH, respectively.

magnetic property of rare-earth Gd ion [48]. Moreover, this parameter further enhances to 3.97 emu/(g·Oe) for the sample of AuNCs/Gd-LDH (Fig. 4B, red line), indicating an improved paramagnetic magnetization after the loading of AuNCs. As discussed above, a significant synergistic effect occurs between AuNCs and Gd-LDH: the electron-transfer from AuNCs to Gd^{3+} leads to an increased Au(I)–thiol concentration and enhanced magnetic susceptibility, which promotes both the fluorescence QY of AuNCs and the longitudinal MR relaxivity of Gd-LDH simultaneously. Such a synergistic effect is rarely documented before.

3.3. In vitro studies

Furthermore, a commonly used photosensitizer (Ce6) was incorporated with AuNCs/Gd-LDH to obtain the final sample Ce6&AuNCs/Gd-LDH, so as to achieve dual-mode imaging and photodynamic therapy. The loading content (LC) and encapsulation efficiency (EE) were studied with the mass ratio of Ce6: LDH ranging from 0.25: 1 to 2: 1 (Fig. S15). Taking into account their balance, the ratio of 1: 1 (LC = 96.9%, EE = 96.9%) was applied in this work. The UV–vis characteristic absorption bands of Ce6 at 400 nm and 660 nm are observed in Ce6&AuNCs/Gd-LDH (Fig. S16A), indicating the successful combination of Ce6 with AuNCs/Gd-LDH. Moreover, since Ce6 with carboxyl groups is negatively-charged, it can be absorbed onto positively-charged Gd-LDH nanosheets. A decrease in zeta potential is demonstrated after the loading of Ce6 onto AuNCs/Gd-LDH: relative to AuNCs/Gd-LDH with a zeta potential of 19.3 mV (Fig. 1G), Ce6&AuNCs/Gd-LDH shows a decreased zeta potential (10.7 mV) due to the electronegativity of Ce6 (−15.7 mV, Fig. S16B). The release amount of Ce6 is below 6.5% in PBS for 24 h, which indicates a good stability of Ce6&AuNCs/Gd-LDH during *in vivo* circulation (Fig. S17). Moreover, the UV–vis spectrum of Ce6&AuNCs/Gd-LDH shows little change within 30 days (Fig. S18), demonstrating a satisfactory storage stability of Ce6 on AuNCs/Gd-LDH under ambient conditions. Ce6&AuNCs/Gd-LDH also displays a satisfactory storage stability in water, PBS and culture medium (Fig. S19A) with rather close size distribution for 30 days (Fig. S19B). The strong Tyndall effect further demonstrates a high aqueous stability and dispersibility of Ce6&AuNCs/Gd-LDH sample as well (Fig. S20). The production efficiency of singlet oxygen, which is a key parameter in photodynamic therapy, was measured by using 1,3-diphenylisobenzofuran (DPBF) as a probe, whose absorption at 410 nm will decrease *via* reaction with singlet oxygen [49]. Fig. S21A shows the decreased intensity of normalized absorbance at 410 nm of DPBF with the presence of pristine Ce6, Ce6&AuNCs and Ce6&AuNCs/Gd-LDH, respectively, upon irradiation at 650 nm. After 8 min irradiation, pristine Ce6 and Ce6&AuNCs show a decrease of 20% and 21%, respectively; in contrast, the sample of Ce6&AuNCs/Gd-LDH displays a decline of 37%, indicating the highest production of singlet oxygen in the case of Ce6&AuNCs/Gd-LDH. This is mainly ascribed to the enhanced anti-photobleaching of Ce6 after incorporation with Gd-LDH (Fig. S21B).

In vitro cellular imaging and PDT performance were performed with HepG2 cells. Fig. 5A shows the fluorescence images of cells incubated with AuNCs, AuNCs/Gd-LDH and Ce6&AuNCs/Gd-LDH for 6 h, respectively. Cells incubated with pristine AuNCs show a weak fluorescence while an obviously increased fluorescence was observed in the groups of AuNCs/Gd-LDH and Ce6&AuNCs/Gd-LDH, indicating an excellent cellular imaging ability of AuNCs after loading onto Gd-LDH nanosheets. Moreover, flow cytometry (Fig. 5B) reveals a 12.5 times enhancement in fluorescence intensity compared with pristine AuNCs, as a result of the largely increased QY of AuNCs/Gd-LDH relative to pristine AuNCs (Fig. 2B). To further evaluate the PDT performance *in vitro*, cells were irradiated at 650 nm with an optical fluence rate of 27 J/cm^2 (15 mW/cm^2, 30 min) after incubation with different dosage of Ce6 and Ce6&AuNCs/Gd-LDH, and Fig. 5C and D shows the cell viability determined by the standard methyl thiazolyl tetrazolium (MTT) assay. Before irradiation, the cell viability treated with 10 μg/mL of Ce6, Ce6&AuNCs and Ce6&AuNCs/Gd-LDH are above 95% (Fig. 5C). After irradiation, cells treated with Ce6 and Ce6&AuNCs with 10 μg/mL show viability of 39% and 35%, respectively (Fig. 5D). In the case of cells treated with Ce6&AuNCs/Gd-LDH, the viability decreases sharply from 100% to 9.2% as the dosage increases from 0 to 10 μg/mL (red bar). Such a promoted anticancer performance of Ce6&AuNCs/Gd-LDH can be ascribed to enhanced permeability and retention (EPR) effect (discussed below) as well as enhanced singlet oxygen production efficiency. The anticancer effect was visualized by using calcein acetoxymethyl ester/propidium iodide (calcein-AM/PI) method, in which dead cells were stained by PI with red fluorescence signal while living cells were stained by calcein-AM with green signal [50]. As shown in Fig. 5E, no cell death is observed for the blank group while Ce6 group shows a few cell mortalities. In contrast, Ce6&AuNCs/Gd-LDH (10 μg/mL) group illustrates a prominent cell death (strong PI signal), consistent with the results of *in vitro* tests. The singlet oxygen production efficiency in cells was evaluated by a chemical staining method using 2′,7′-dichlorodihydrofluorescein diacetate (DCFH-DA) [51], which shows green fluorescence signal after reacting with singlet oxygen. As shown in Fig. 5F, cells treated with Ce6&AuNCs/Gd-LDH exhibits the strongest signal, indicating the highest ROS production. Moreover, flow cytometry measurement was applied to quantify the singlet oxygen production (Fig. 5G), and the results showed the group treated with Ce6&AuNCs/Gd-LDH (red peak) gives 11.7 times promoted signal intensity than the group of Ce6 (green peak).

3.4. In vivo imaging and cancer therapy

In vivo MRI performance of Ce6&AuNCs/Gd-LDH and Gd-LDH was evaluated by mice bearing HepG2 tumor. As the tumor volume reached ~70 mm^3, the mice were administered with an intravenous (*i.v.*) injection of Ce6&AuNCs/Gd-LDH and Gd-LDH with an equivalent dose of Gd (0.88 mg/kg of mouse weight), respectively. T_1-weighted MR images were collected within 0–48 h after injection. For Ce6&AuNCs/Gd-LDH sample (Fig. 6A), the T_1-weighted MR signal in the tumor area increases gradually after *i.v.* injection and reached the highest level at 12 h, indicating that Ce6&AuNCs/Gd-LDH accumulates constantly at the tumor site for the first 12 h due to the enhanced EPR effect. Afterwards, the MR signal decreases gradually from 12 h to 48 h. Compared with the commercial Gd-based contrast agents (less than 2 h), the prolonged MR imaging time suggests potential application of Ce6&AuNCs/Gd-LDH in diagnosis. In comparison, mice injected with Gd-LDH show the same trend but with relatively weaker MR signal intensity (Fig. S22). The promoted *in vivo* MRI performance of Ce6&AuNCs/Gd-LDH relative to pristine Gd-LDH can be ascribed to the enhanced r_1 value, which has been discussed above.

In vivo fluorescence imaging of Ce6&AuNCs/Gd-LDH was studied through intratumor injection, due to the limited tissue penetration of excitation wavelength (410 nm). Mice injected intratumorly with pristine AuNCs showed no signal due to the weak luminescence efficiency and insufficient internal penetration (Fig. S23). In contrast, intense signal was observed at the mice treated with Ce6&AuNCs/Gd-LDH after 0.1 h injection (Fig. 6B) and remained constant for 6 h. Subsequently, the fluorescence signal expanded from the center and faded away gradually from 6 to 24 h, illustrating a good stability and clearance ability of Ce6&AuNCs/Gd-LDH. The largely promoted fluorescence QY of Ce6&AuNCs/Gd-LDH

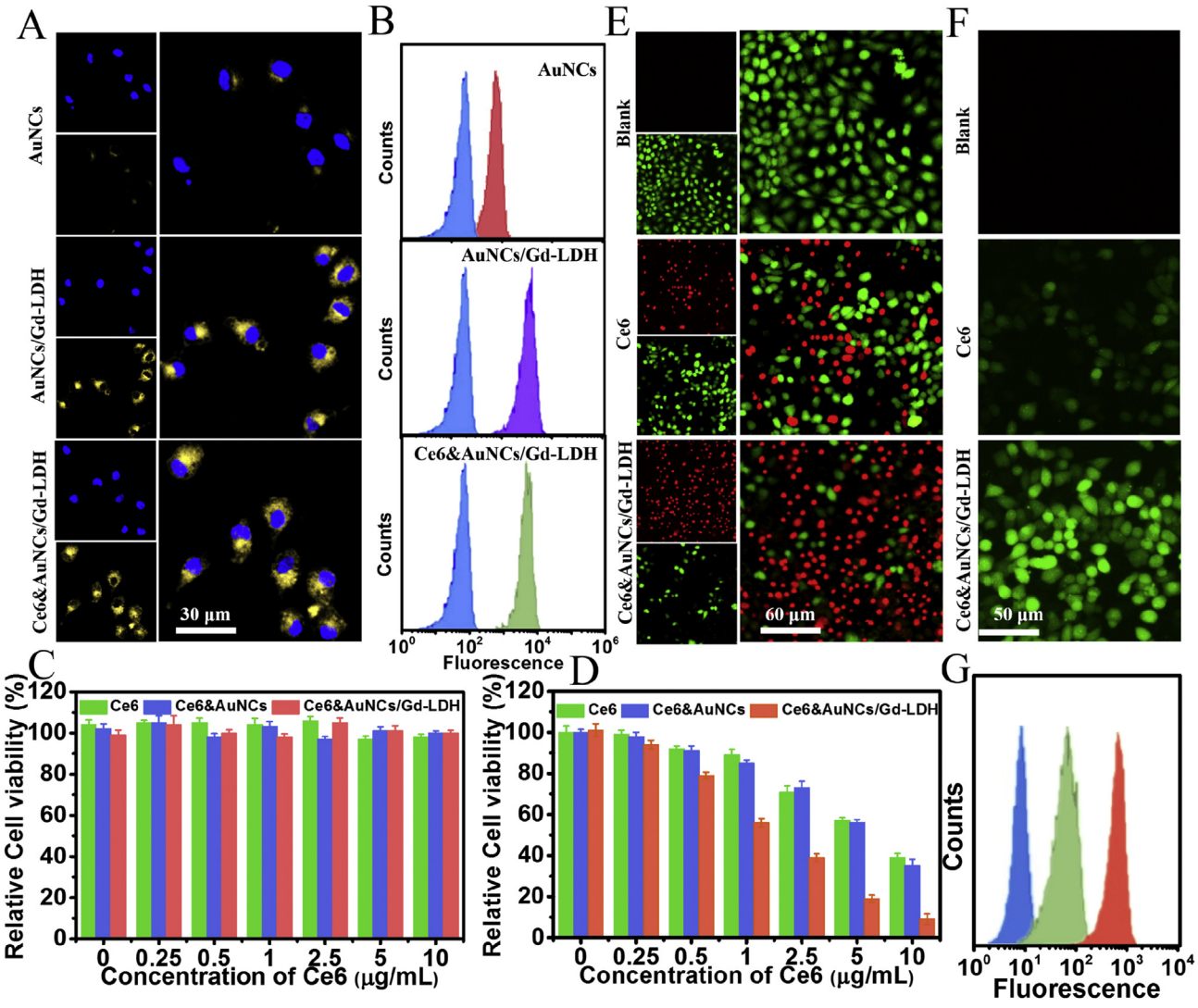

Fig. 5. (A) Confocal fluorescence images of HepG2 cells incubated with AuNCs, AuNCs/Gd-LDH and Ce6&AuNCs/Gd-LDH for 6 h (equivalent AuNCs: 10 μg/mL), respectively. (B) Flow cytometry measurement of cellular fluorescence treated with AuNCs, AuNCs/Gd-LDH and Ce6&AuNCs/Gd-LDH, respectively. MTT assay of cell viabilities after incubation with free Ce6, Ce6&AuNCs and Ce6&AuNCs/Gd-LDH (C) before irradiation and (D) after irradiation (650 nm; 15 mW/cm^2). (E) Confocal fluorescence images of cells incubated with free Ce6, Ce6&AuNCs and Ce6&AuNCs/Gd-LDH with irradiation, stained with calcium AM and PI. (F) Intracellular ROS production treated with different samples using DCFH-DA as a probe. (G) Flow cytometry measurement of DCFH-DA signal for blank (blue), Ce6 (green) and Ce6&AuNCs/Gd-LDH (red). (For interpretation of the references to colour in this figure legend, the reader is referred to the Web version of this article.)

relative to pristine AuNCs (18.5% *vs.* 3.1%) (Fig. S24), is responsible for its superior *in vivo* fluorescence image ability. Moreover, to study the biodistribution of Ce6&AuNCs/Gd-LDH, mice were injected intravenously and main organs were collected at different time points. Fig. S25A and B show the biodistribution and averaged fluorescence intensity of various organs at 2 h, 8 h, 12 h, 24 h and 48 h. The strongest fluorescence intensity of tumor is found at 12 h, which accords with the MRI results.

Based on the effective accumulation of Ce6&AuNCs/Gd-LDH within tumor site, *in vivo* antitumor performance of Ce6&AuNCs/Gd-LDH was evaluated. The treated mice were *i.v.* injected with a drug dose of 2 mg/kg (200 μL) followed by a 650 nm irradiation (15 mW/cm^2, 30 min) or without irradiation at 12 h post injection. The volume changes of tumor were monitored over 16 d and Fig. 6C displays the tumor growth curves of mice after various treatments. The saline with/without irradiation as well as Ce6 and Ce6&AuNCs/Gd-LDH group without irradiation show negligible tumor inhibition; mice treated with Ce6 upon irradiation partially inhibits the tumor growth. In contrast, Ce6&AuNCs/Gd-LDH upon irradiation produces the most efficient inhibition of tumor growth compared with the control groups, resulting from the EPR effect and enhanced PDT efficiency. The digital photos of the mice and corresponding excised tumors (Fig. 6D) visually illuminate that the tumor size treated with Ce6&AuNCs/Gd-LDH plus irradiation is significantly smaller than the other groups. Hematoxylin and eosin (H&E) staining analysis shows that severe tumor tissues necrosis and cell shrinkage are observed in the group of Ce6&AuNCs/Gd-LDH with laser irradiation while only partial necrosis or no damage can be seen in the control groups (Fig. 6E). In addition, *in vivo* toxicity of Ce6&AuNCs/Gd-LDH was evaluated by histological analysis of main organs, blood biochemistry as well as liver and kidney function markers. The H&E analysis of major organs (heart, liver, spleen, lung, and kidney) (Fig. S26) shows no significant damage in Ce6&AuNCs/Gd-LDH and saline group. The blood biochemistry indices (WBC, RBC, HGB and PLT), as well as the liver and kidney function indices (AST, ALT BUN and CRE), gave no obvious

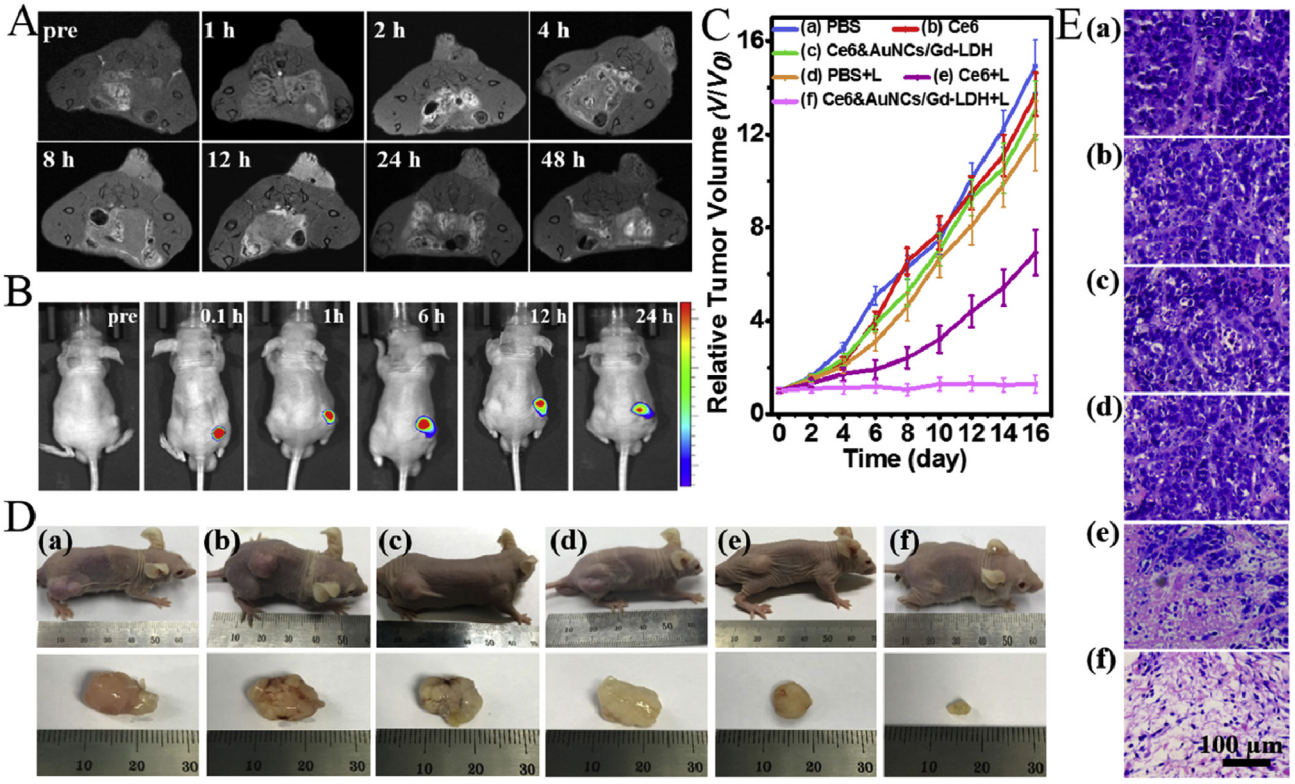

Fig. 6. (A) *In vivo* MR imaging of HepG2 tumor-bearing nude mouse taken at different time points post intravenous injection of Ce6&AuNCs/Gd-LDH. (B) *In vivo* fluorescence imaging of mouse after intratumoral injection of Ce6&AuNCs/Gd-LDH. (C) Tumor growth curves of mice after various treatments indicated ($n = 6$ per group). (D) Representative photos of mice with corresponding tumor and (E) H&E stained tumor tissue slices after 16 d treatments with: (a) PBS, (b) Ce6, (c) Ce6&AuNCs/Gd-LDH, (d) PBS with irradiation, (e) Ce6 with irradiation, (f) Ce6&AuNCs/Gd-LDH with irradiation.

difference after 1 day and 7 days between Ce6&AuNCs/Gd-LDH and saline group (Fig. S27). The results above demonstrate that Ce6&AuNCs/Gd-LDH does not show obvious side effect and can be used as a safe theranostics candidate for *in vivo* application.

4. Conclusion

In conclusion, we developed an MR/FL dual-modality imaging guided photodynamic therapy system based on loading AuNCs and Ce6 on the surface of Gd-LDH monolayer nanosheets. The QY of Ce6&AuNCs/Gd-LDH enhances to 18.5% compared with pristine AuNCs (3.1%); moreover, Ce6&AuNCs/Gd-LDH exhibits superior T_1-MRI performance ($r_1 = 17.57\ mM^{-1}s^{-1}$) than that of commercially used MRI contrast agent Gd-DOTA ($r_1 \approx 3.4\ mM^{-1}s^{-1}$), demonstrating a synergistic effect between AuNCs and Gd-LDH. In addition, an excellent MR/FL dual-modality imaging guided cancer therapy was demonstrated both *in vitro* and *in vivo*: an efficient inhibition of tumor growth can be achieved with a drug dose of 2 mg/kg (650 nm irradiation; optical fluence rate: 27 J/cm^2). Therefore, this work demonstrates an MR/FL dual-modality imaging guided photodynamic therapy by using a highly integrated nanomaterial, which shows great potential application as a theranostic agent against cancer.

Conflicts of interest

The authors declare no competing financial interest.

Acknowledgments

This work was supported by the National Natural Science Foundation of China (NSFC), the 973 Program (2014CB932102), the Beijing Natural Science Foundation (2174082 and 7162092), the Fundamental Research Funds for the Central Universities (buctylkxj01) and the National Great New Drugs Development Project of China (2017ZX09301-040).

Appendix A. Supplementary data

Supplementary data related to this article can be found at https://doi.org/10.1016/j.biomaterials.2018.02.032.

References

[1] D. Peer, J.M. Karp, S. Hong, O.C. Farokhzad, R. Margalit, R. Langer, Nanocarriers as an emerging platform for cancer therapy, Nat. Nanotechnol. 2 (2007) 751–760.
[2] Y. Sun, X. Zhu, J. Peng, F. Li, Core–shell lanthanide upconversion nanophosphors as four-modal probes for tumor angiogenesis imaging, ACS Nano 7 (12) (2013) 11290–11300.
[3] D.-H. Park, J.-E. Kim, J.-M. Oh, Y.-G. Shul, J.-H. Choy, DNA core@inorganic shell, J. Am. Chem. Soc. 132 (47) (2010) 16735–16736.
[4] J. Peng, L. Zhao, X. Zhu, Y. Sun, W. Feng, Y. Gao, L. Wang, F.Y. Li, Hollow silica nanoparticles loaded with hydrophobic phthalocyanine for near-infrared photodynamic and photothermal combination therapy, Biomaterials 34 (32) (2013) 7905–7912.
[5] Q. Yao, X. Yuan, V. Fung, Y. Yu, D.T. Leong, D.-E. Jiang, J. Xie, Understanding seed-mediated growth of gold nanoclusters at molecular level, Nat. Commun. 8 (2017) 927.
[6] L.A. Dykman, N.G. Khlebtsov, Multifunctional gold-based nanocomposites for theranostics, Biomaterials 108 (2016) 13–34.
[7] Y. Yang, Q. Zhao, W. Feng, F.Y. Li, Luminescent chemodosimeters for bioimaging, Chem. Rev. 113 (1) (2013) 192–270.
[8] K. Zheng, M.I. Setyawati, D.T. Leong, J. Xie, Antimicrobial gold nanoclusters, ACS Nano 11 (7) (2017) 6904–6910.
[9] X. Gu, R.T.K. Kwok, J.W.Y. Lam, B.Z. Tang, AIEgens for biological process monitoring and disease theranostics, Biomaterials 146 (2017) 115–135.

[10] M.S. Muthu, R.V. Kutty, Z. Luo, J. Xie, S.-S. Feng, Theranostic vitamin E TPGS micelles of transferrin conjugation for targeted co-delivery of docetaxel and ultra bright gold nanoclusters, Biomaterials 39 (2015) 234–248.
[11] R.Z. Liang, M. Wei, D.G. Evans, X. Duan, Inorganic nanomaterials for bioimaging, targeted drug delivery and therapeutics, Chem. Commun. (J. Chem. Soc. Sect. D) 50 (91) (2014) 14071–14081.
[12] Y.B. Fan, C.Y. Li, F.Y. Li, D.Y. Chen, pH-activated size reduction of large compound nanoparticles for *in vivo* nucleus-targeted drug delivery, Biomaterials 85 (2016) 30–39.
[13] X.-D. Zhang, Z. Luo, J. Chen, X. Shen, S. Song, Y. Sun, S. Fan, F. Fan, D.T. Leong, J. Xie, Ultrasmall $Au_{10-12}(SG)_{10-12}$ nanomolecules for high tumor specificity and cancer radiotherapy, Adv. Mater. 26 (26) (2014) 4565–4568.
[14] Q. Liu, Y. Sun, C. Li, J. Zhou, C. Li, T. Yang, X. Zhang, T. Yi, D. Wu, F.Y. Li, ^{18}F-labeled magnetic-upconversion nanophosphors via rare-earth cation-assisted ligand assembly, ACS Nano 5 (4) (2011) 3146–3157.
[15] R. Kojima, D. Aubel, M. Fussenegger, Toward a world of theranostic medication: programming biological sentinel systems for therapeutic intervention, Adv. Drug Deliv. Rev. 105 (2016) 66–76.
[16] K. Yang, G. Yang, L. Chen, L. Cheng, L. Wang, C. Ge, Z. Liu, FeS nanoplates as a multifunctional nano-theranostic for magnetic resonance imaging guided photothermal therapy, Biomaterials 38 (2015) 1–9.
[17] R. Kumar, J. Han, H.J. Lim, W.X. Ren, J.Y. Lim, J.H. Kim, J.S. Kim, Mitochondrial induced and self-monitored intrinsic apoptosis by antitumor theranostic prodrug: *in vivo* imaging and precise cancer treatment, J. Am. Chem. Soc. 136 (51) (2014) 17836–17843.
[18] H. Yang, H. Mao, Z. Wan, A. Zhu, M. Guo, Y. Li, X. Li, J. Wan, X. Yang, X. Shuai, H. Chen, Micelles assembled with carbocyanine dyes for theranostic near-infrared fluorescent cancer imaging and photothermal therapy, Biomaterials 34 (36) (2013) 9124–9133.
[19] Y.W. Chen, T.Y. Liu, P.J. Chen, P.H. Chang, S.Y. Chen, A high-sensitivity and low-power theranostic nanosystem for cell SERS imaging and selectively photothermal therapy using anti-EGFR-conjugated reduced graphene oxide/mesoporous silica/AuNPs nanosheets, Small 12 (11) (2016) 1458–1468.
[20] C. Tan, P. Yu, Y. Hu, J. Chen, Y. Huang, Y. Cai, Z. Luo, B. Li, Q. Lu, L. Wang, Z. Liu, H. Zhang, High-yield exfoliation of ultrathin two-dimensional ternary chalcogenide nanosheets for highly sensitive and selective fluorescence DNA sensors, J. Am. Chem. Soc. 137 (32) (2015) 10430–10436.
[21] R.C. Lv, D. Yang, P.P. Yang, J.T. Xu, F. He, S.L. Gai, C.X. Li, Y.L. Dai, G.X. Yang, J. Lin, Integration of upconversion nanoparticles and ultrathin black phosphorus for efficient photodynamic theranostics under 808 nm near-infrared light irradiation, Chem. Mater. 28 (13) (2016) 4724–4734.
[22] Y. Chen, D.L. Ye, M.Y. Wu, H.R. Chen, L.L. Zhang, J.L. Shi, L.Z. Wang, Break-up of two-dimensional MnO_2 nanosheets promotes ultrasensitive pH-triggered theranostics of cancer, Adv. Mater. 26 (41) (2014) 7019–7026.
[23] X.Q. Qian, X.X. Han, Y. Chen, Insights into the unique functionality of inorganic micro/nanoparticles for versatile ultrasound theranostics, Biomaterials 142 (2017) 13–30.
[24] L. Cheng, J. Liu, X. Gu, H. Gong, X. Shi, T. Liu, C. Wang, X. Wang, G. Liu, H. Xing, W. Bu, B. Sun, Z. Liu, PEGylated WS_2 nanosheets as a multifunctional theranostic agent for *in vivo* dual-modal CT/photoacoustic imaging guided photothermal therapy, Adv. Mater. 26 (12) (2014) 1886–1893.
[25] K. Ladewig, Z.P. Xu, G.Q. Lu, Layered double hydroxide nanoparticles in gene and drug delivery, Expet Opin. Drug Deliv. 6 (9) (2009) 907–922.
[26] B. Li, Z. Gu, N. Kurniawan, W. Chen, Z.P. Xu, Manganese-based layered double hydroxide nanoparticles as a T-1 MRI contrast agent with ultrasensitive pH response and high relaxivity, Adv. Mater. 29 (29) (2017) 1700373–1700381.
[27] R.Z. Liang, R. Tian, L.N. Ma, L.L. Zhang, Y. Hu, J. Wang, M. Wei, D. Yan, D.G. Evans, X. Duan, A supermolecular photosensitizer with excellent anticancer performance in photodynamic therapy, Adv. Funct. Mater. 24 (21) (2014) 3144–3151.
[28] J.-H. Choy, S.-Y. Kwak, Y.-J. Jeong, J.-S. Park, Inorganic layered double hydroxides as nonviral vectors, Angew. Chem. Int. Ed. 39 (22) (2000) 4041–4045.
[29] D.P. Yan, J. Lu, J. Ma, M. Wei, D.G. Evans, X. Duan, Reversibly thermochromic, fluorescent ultrathin films with a supramolecular architecture, Angew. Chem. Int. Ed. 50 (3) (2011) 720–723.
[30] Q. Wang, S.V. Tang, E. Lester, D. O'Hare, Synthesis of ultrafine layered double hydroxide (LDHs) nanoplates using a continuous-flow hydrothermal reactor, Nanoscale 5 (1) (2013) 114–117.
[31] Q. Wang, D. O'Hare, Recent advances in the synthesis and application of layered double hydroxide (LDH) nanosheets, Chem. Rev. 112 (7) (2012) 4124–4155.
[32] Y.F. Zhao, G. Chen, T. Bian, C. Zhou, G.I. Waterhouse, L.Z. Wu, C.H. Tung, L.J. Smith, D. O'Hare, T. Zhang, Defect-rich ultrathin ZnAl-layered double hydroxide nanosheets for efficient photoreduction of CO_2 to CO with water, Adv. Mater. 27 (47) (2015) 7824–7831.
[33] M.-Q. Zhao, Q. Zhang, J.-Q. Huang, F. Wei, Hierarchical nanocomposites derived from nanocarbons and layered double hydroxides-properties, synthesis, and applications, Adv. Funct. Mater. 22 (4) (2012) 675–694.
[34] M.F. Shao, Z.H. Li, R.K. Zhang, F.Y. Ning, M. Wei, D.G. Evans, X. Duan, Hierarchical conducting polymer@clay core-shell arrays for flexible all-solid-state supercapacitor devices, Small 11 (29) (2015) 3530–3538.
[35] R. Tian, D.P. Yan, C.Y. Li, S.M. Xu, R.Z. Liang, L.Y. Guo, M. Wei, D.G. Evans, X. Duan, Surface-confined fluorescence enhancement of Au nanoclusters anchoring to a two-dimensional ultrathin nanosheet toward bioimaging, Nanoscale 8 (18) (2016) 9815–9821.
[36] S.H. Koenig, R.D. Brown, Field-cycling relaxometry of protein solutions and tissue: implications for MRI, Prog. Nucl. Magn. Reson. Spectrosc. 22 (6) (1990) 487–567.
[37] Y.-S. Chen, H. Choi, P.V. Kamat, Metal-cluster-sensitized solar cells. A new class of thiolated gold sensitizers delivering efficiency greater than 2%, J. Am. Chem. Soc. 135 (24) (2013) 8822–8825.
[38] A. Beeby, I.M. Clarkson, R.S. Dickins, S. Faulkner, D. Parker, L. Royle, A.S. de Sousa, J.A. Gareth Williams, M. Woods, Non-radiative deactivation of the excited states of europium, terbium and ytterbium complexes by proximate energy-matched OH, NH and CH oscillators: an improved luminescence method for establishing solution hydration states, J. Chem. Soc. Perkin Trans. 2 (3) (1999) 493–504.
[39] Q.G.D. Lussanet, S. Langereis, R.G.H. Beets-Tan, M.H.P.V. Genderen, A.W. Griffioen, J.M.A.V. Engelshoven, W.H. Backes, Dynamic contrast-enhanced MR imaging kinetic parameters and molecular weight of dendritic contrast agents in tumor angiogenesis in mice, Radiology 235 (1) (2005) 65–72.
[40] F. Song, X.L. Hu, Exfoliation of layered double hydroxides for enhanced oxygen evolution catalysis, Nat. Commun. 5 (2014) 4477.
[41] H. Ito, T. Saito, N. Oshima, N. Kitamura, S. Ishizaka, Y. Hinatsu, M. Wakeshima, M. Kato, K. Tsuge, M. Sawamura, Reversible mechanochromic luminescence of $[(C_6F_5Au)_2(\mu\text{-}1,4\text{-Diisocyanobenzene})]$, J. Am. Chem. Soc. 130 (31) (2008) 10044–10045.
[42] S.-H. Cha, J.-U. Kim, K.-H. Kim, J.-C. Lee, Preparation and photoluminescent properties of Gold(I)–alkanethiolate complexes having highly ordered supramolecular structures, Chem. Mater. 19 (25) (2007) 6297–6303.
[43] Z. Luo, X. Yuan, Y. Yu, Q. Zhang, D.T. Leong, J.Y. Lee, J. Xie, From aggregation-induced emission of Au(I)–thiolate complexes to ultrabright Au(0)@Au(I)–thiolate core–shell nanoclusters, J. Am. Chem. Soc. 134 (40) (2012) 16662–16670.
[44] R.M. Supkowski, W.D. Horrocks, On the determination of the number of water molecules, *q*, coordinated to europium(III) ions in solution from luminescence decay lifetimes, Inorg. Chim. Acta. 340 (2002) 44–48.
[45] J.L. Major, R.M. Boiteau, T.J. Meade, Mechanisms of ZnII-activated magnetic resonance imaging agents, Inorg. Chem. 47 (22) (2008) 10788–10795.
[46] W.D. Horrocks, D.R. Sudnick, Lanthanide ion luminescence probes of the structure of biological macromolecules, Acc. Chem. Res. 14 (12) (1981) 384–392.
[47] W.D. Horrocks, D.R. Sudnick, Lanthanide ion probes of structure in biology. Laser-induced luminescence decay constants provide a direct measure of the number of metal-coordinated water molecules, J. Am. Chem. Soc. 101 (2) (1979) 334–340.
[48] V.S. Marangoni, O. Neumann, L. Henderson, C.C. Kaffes, H. Zhang, R. Zhang, S. Bishnoi, C. Ayala-Orozco, V. Zucolotto, J.A. Bankson, P. Nordlander, N.J. Halas, Enhancing T1 magnetic resonance imaging contrast with internalized gadolinium(III) in a multilayer nanoparticle, Proc. Natl. Acad. Sci. Unit. States Am. 114 (27) (2017) 6960–6965.
[49] Z. Hou, Y. Zhang, K. Deng, Y. Chen, X. Li, X. Deng, Z. Cheng, H. Lian, C. Li, J. Lin, UV-emitting upconversion-based TiO_2 photosensitizing nanoplatform: near-infrared light mediated *in vivo* photodynamic therapy via mitochondria-involved apoptosis pathway, ACS Nano 9 (3) (2015) 2584–2599.
[50] F. Liu, X. He, H. Chen, J. Zhang, H. Zhang, Z. Wang, Gram-scale synthesis of coordination polymer nanodots with renal clearance properties for cancer theranostic applications, Nat. Commun. 6 (2015) 8003.
[51] Z.H. Xiang, L. Zhu, L. Qi, L. Yan, Y.H. Xue, D. Wang, J.-F. Chen, L.M. Dai, Two-dimensional fully conjugated polymeric photosensitizers for advanced photodynamic therapy, Chem. Mater. 28 (23) (2016) 8651–8658.